Development of a light scattering solver applicable to particles of arbitrary shape on the basis of the surface-integral equations method of Müller type. I. Methodology, accuracy of calculation, and electromagnetic current on the particle surface

Takashi Y. Nakajima,[1,2,*] Teruyuki Nakajima,[3] Kyu Yoshimori,[4] Sumit K. Mishra,[5] and Sachchida N. Tripathi[5]

[1]Research and Information Center, Tokai University, 2-28-4 Tomigaya, Shibuya-ku, Tokyo 151-0063, Japan

[2]Department of Atmospheric Sciences, Colorado State University, 1371 Campus Delivery, Fort Collins, Colorado 80523-1371, USA

[3]Center for Climate System Research, University of Tokyo, 5-1-5 Kashiwanoha, Kashiwa, Chiba 277-8568, Japan

[4]Department of Computer and Information Science, Iwate University, 4-3-5 Ueda, Morioka, Iwate 020-8551, Japan

[5]Department of Civil Engineering, Indian Institute of Technology Kanpur, India, 208016, India

*Corresponding author: nkjm@yoyogi.ycc.u-tokai.ac.jp

We develop a numerical algorithm for calculating the light-scattering properties of small particles of arbitrary shape on the basis of a method involving surface integral equations. The calculation error was estimated by performing a comparison between the proposed method and the exact Mie method with regard to the extinction efficiency factor, and the results show that the error is less than 1% when four or more nodes per wavelength are set on the surface of a spherical particle. The accuracy fluctuates in accordance with the distribution of nodal points on the particle surface with respect to the direction of propagation of the incident light. From our examinations, it is shown that the polar incidence alignment yields higher accuracy than equator incidence when a "latitude–longitude" type of mesh generation is adopted. The electric currents on the particle surface and the phase functions of all scattering directions are shown for particles shaped as spheres or hexagonal columns. It is shown that the phase function for a hexagonal column has four or eight cold spots. The phase function of a randomly oriented hexagonal column shows halolike peaks with size parameters of up to 20. This method can be applied to particles with a size parameter of up to about 20 without using the symmetry characteristic of the particle. © 2009 Optical Society of America

OCIS codes: 010.0010, 290.5850, 290.5825, 280.0280, 280.1310.

1. Introduction

Light scattering by small particles is an important research subject in many scientific and engineering fields, such as astronomy and geophysics. For example, in Earth observation and remote sensing with spaceborne satellites, it is necessary to calculate the radiative transfer, which includes scattering of electromagnetic waves by particles in the atmosphere, such as clouds and aerosols, in addition to scattering from molecules and interactions at the ground surface. In fact, many radiative transfer solvers have been used for simulating

satellite-measured signals with respect to such complex scattering processes. In such calculations, it is necessary to consider that, generally, the shape of most scattering particles in nature is nonspherical, with the exception of particular types of particles, such as warm water cloud droplets. Thus, an efficient and accurate method for calculating the light-scattering properties of nonspherical particles has been pursued for many years. In the context of this paper, the term "scattering properties" denotes the efficiency factors of the scattering and the phase function.

There are two possible approaches to obtaining the light-scattering properties for nonspherical particles. One approach is based on an approximation method, while the other involves an exact solution. A typical method used in the former approach is an algorithm based on the geometrical optics approximation (GOA), which is applicable to particles with very large size parameters ($\alpha = 2\pi r/\lambda$, where r is the *equivalent-volume-sphere radius* of the nonspherical particle and λ is the wavelength of the incident light). Liou and Takano [1] applied GOA to homogeneous hexagonal columns, hollow columns, bullet rosettes, dendrites, and capped columns. The method has also been applied to more complex shapes, such as polyhedral ice crystals [2] and randomly shaped rough particles [3,4]. Although the GOA technique has a long history, it is still valuable for estimating the appearance of visible optical phenomena, such as halos and/or arcs, in the results of exact methods [5,6], as well as for calculating the scattering properties for large particles [7]. The most precise theories and numerical algorithms corresponding to the latter approach are based on solving Maxwell's equations. Analytical solutions have been examined for only a few simple cases. Mie [8] derived a solution for homogeneous isotropic spheres, while Wait [9] obtained a full solution for infinite homogenous isotropic circular cylinders. Furthermore, Asano and Yamamoto [10] successfully derived a general solution for homogeneous isotropic spheroids. In addition to exact *analytical* solutions, many *numerical* algorithms have also been developed for solving this problem. The T-matrix method [11,12] and the finite-difference time-domain (FDTD) method [13] are two efficient methods for performing such calculations, and a comprehensive scattering database has been developed by using a combination of FDTD, T-matrix, and GOA [7]. Among the numerical algorithms, methods based on volume or surface integrals are considered to be efficient for such calculations. One of the popular algorithms for methods based on volume-integral equations, which are applicable to particles of arbitrary shapes, is discrete dipole approximation (DDA) [14,15]. This method involves partitioning a particle into N dipoles. However, since N is proportional to α^3, in principle, the computing time drastically increases following the increase of α. On the contrary, a method based on surface integral equations requires less computational resources

than that based on volume integral equations since the number of matching nodal points (NMNP) is proportional to α^2. Mano [16] developed an algorithm for a method based on surface-integral equations and obtained the scattering properties for a homogeneous hexagonal column with a size parameter of up to 40. FDTD can be applied to both the volume- and surface-integral methods [17]. Results obtained from several methods have been used for the data analysis of atmospheric observations. For example, Dubovik [18] applied nonspherical models to the Aerosol Robotic Network (AERONET) sky-radiometer data and showed that the mixture of spheroids allows accurate fitting of measured spectral and angular dependencies of observed intensity and polarization.

We have focused on developing an algorithm, the surface-integral equation method for Müller type (SIEM/M), for a method based on surface-integral equations. The target particles are shaped as spheres or hexagonal columns in this paper. There are three objectives in this paper. The first is the elucidation of the relationship between the accuracy of the obtained scattering properties and NMNP. Regarding this objective, Mano [16] has shown that six nodes per wavelength are necessary in order to obtain the scattering properties with very high accuracy. He used the symmetry characteristic of hexagonal particles in order to drastically reduce the required computational resources (both the calculation time and the amount of required memory). Since one of the aims of this paper is the elucidation of the applicability of the method based on surface-integral equations to particles with arbitrary shapes with limited computer resources, we do not use the symmetry of the particles. Thus, the number of nodes per wavelength is set to less than six in some calculations. Although this might degrade the calculation accuracy or restrict the calculations to smaller values of the size parameter as compared with those in Mano [16], the results provide significant indications when the method based on surface-integral equations is adopted to particles of arbitrary shape, which entail higher requirements for computer memory. The second objective is the derivation of the electromagnetic currents on the surface of scattering particles and the scattering phase functions for all scattering directions. The results reveal the importance of the smoothness of the electromagnetic currents on the surface of the particle with respect to obtaining the scattering parameters with high accuracy. Finally, the phase functions of randomly oriented hexagonal column particles are presented and discussed.

2. Formulations and Numerical Calculation Method

A. Combined Surface-Integral Equations of the Müller type

In this section, we introduce an integral equation method based on obtaining numerical solutions of Maxwell's equations. The important advantage of

surface-integral equations is that the dimensionality of the problem is reduced by 1 as compared to the case of volume-integral equations, and the number of unknowns is proportional to the square rather than to the cube of the particle size. We chose Fredholm equations of the second kind, which were obtained by Müller [19]. These equations are based on the following formulations:

$$
\mathbf{i}(\mathbf{r}) \times \mathbf{E}_{\text{inc}}(\mathbf{r}) = -\frac{1}{2}(\tilde{m}^2 + 1)\mathbf{K}(\mathbf{r}) - \mathbf{i}(\mathbf{r})
$$
$$
\times \int_s \{jk_0^2 \mathbf{J}(\mathbf{r}')(\tilde{m}^2 G_1 - G_0) + k_0 \mathbf{K}(\mathbf{r}')
$$
$$
\times \nabla'(\tilde{m}^2 G_1 - G_0) + j(\mathbf{J}(\mathbf{r}')
$$
$$
\cdot \nabla')\nabla'(G_1 - G_0)\}\mathrm{d}s', \tag{1}
$$

$$
\mathbf{i}(\mathbf{r}) \times \mathbf{H}_{\text{inc}}(\mathbf{r}) = \mathbf{J}(\mathbf{r}) - \mathbf{i}(\mathbf{r})
$$
$$
\times \int_s \{jk_0^2 \mathbf{K}(\mathbf{r}')(\tilde{m}^2 G_1 - G_0) - k_0 \mathbf{J}(\mathbf{r}')
$$
$$
\times \nabla'(G_1 - G_0)
$$
$$
+ j(\mathbf{K}(\mathbf{r}') \cdot \nabla')\nabla'(G_1 - G_0)\}\mathrm{d}s', \tag{2}
$$

where $\mathbf{r}$ and $\mathbf{r}'$ are the positions of matching and integration points, respectively. $\mathbf{E}_{\text{inc}}$ and $\mathbf{H}_{\text{inc}}$ denote the incident plane electromagnetic wave. $\mathbf{J}$ and $\mathbf{K}$ are unknown surface electric and magnetic currents at $\mathbf{r}$, j is the imaginary unit, $\tilde{m}$ is the complex refractive index of the scattering particle, $\mathbf{i}$ is an outward unit vector normal to the surface of the scattering particle at $\mathbf{r}$, and k_0 is the wavenumber of the incident electromagnetic wave. G_1 and G_0 represent the Green's function of the three-dimensional Helmholtz equation for the incident wavenumber k_0 for the inside (subindex of 1) and the outside (subindex of 0) of the scattering object:

$$
G_1(\mathbf{r}, \mathbf{r}') = \frac{e^{-j\tilde{m}k_0|\mathbf{r}-\mathbf{r}'|}}{4\pi k_0|\mathbf{r}-\mathbf{r}'|}, \tag{3}
$$

$$
G_0(\mathbf{r}, \mathbf{r}') = \frac{e^{-jk_0|\mathbf{r}-\mathbf{r}'|}}{4\pi k_0|\mathbf{r}-\mathbf{r}'|}. \tag{4}
$$

B. Methodology of Numerical Calculation

For the numerical calculation, $\mathbf{J}$ and $\mathbf{K}$ are discretized as

$$
\mathbf{J}(\mathbf{r}) = \sum_{m=1}^{M} \mathbf{a}_m f_m(\mathbf{r}), \tag{5}
$$

$$
\mathbf{K}(\mathbf{r}) = \sum_{m=1}^{M} \mathbf{b}_m f_m(\mathbf{r}), \tag{6}
$$

where $f_m(\mathbf{r})$ is the local-domain basis function with number of $M = 100$ ($10 \times 10 = 100$ around the integral point). We adopted the three-dimensional B-spline function for f. Equations (1) and (2) can be discretized and written by using residual equations. In our calculations, a point matching method is adopted.

The coordinates of every nodal point are expressed as $\mathbf{r}(x, y, z) = \mathbf{r}(s, t)$. Here, $\mathbf{r}$ is parametrically represented by $\mathbf{r}(s, t) = (x(s, t), y(s, t), z(s, t))$, where s and t are scalar parameters along the latitudinal and longitudinal curves on the surface of particles. Figure 1 schematically illustrates the "latitude–longitude" type of particle definition with s and t as parameters and presents a parametrical illustration of the defined particle surface for a sphere and a hexagonal column. In this example, the number of points defined along the s and t curves is 19 and 24 for the sphere and 25 and 24 for the hexagonal column and, thus, the surface currents $\mathbf{J}$ and $\mathbf{K}$ are set at $19 \times 24 = 456$ and $25 \times 24 = 600$ NMNP for the sphere and the hexagonal column in these cases. The small surface facet used for integrating Eqs. (1) and (2) can be described by means of a Jacobian and $\mathrm{d}s\mathrm{d}t$:

$$
\Delta s' = \left| \frac{\partial \mathbf{r}'(s, t)}{\partial s} \times \frac{\partial \mathbf{r}'(s, t)}{\partial t} \right| \mathrm{d}s\mathrm{d}t. \tag{7}
$$

The Gaussian quadrature integration was applied to avoid the singular point that appeared when $|\mathbf{r} - \mathbf{r}'| = 0$ in the Green's function. In fact, dense and coarse numerical integrations had been performed around and far from the target matching nodal point $\mathbf{r}$. The number of Gauss points along both the s and t parameters were 20 at the four meshes that surround the target matching nodal point $\mathbf{r}$, and 4 at the other meshes.

The definition of particles (generally, "mesh generation") can be accomplished with ease in our computation program. First, the user is required to set the position of the nodes by using an (x, y, z) coordinate system. At this time, only the minimal number of nodes sufficient for representing the framework of the particle (referred to as "fundamental nodes") is necessary. Users can add more nodes ("additional
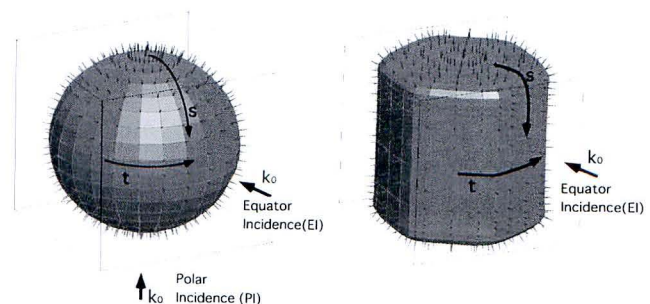

Fig. 1. Models of a sphere and a hexagonal column with normal vectors at all matching nodal points. A parametric spline is used for defining the particle size. k_0 denotes the incident wavenumber.

nodes") between every fundamental node by simply defining the number of divisions between fundamental nodes. When the user wishes to distort the shape of the particle, it is necessary to alter the coordinates of one or more fundamental nodes. The three-dimensional parametric spline function connects all fundamental and additional nodes smoothly, regardless of whether the user has implemented any distortions. This simple method of particle definition allows us to generate particles with arbitrary shapes in a few simple steps.

Equations (1) and (2) can be expressed as algebraic equations for solving $\mathbf{a}_m$ and $\mathbf{b}_m$ in Eqs. (5) and (6):

$$\mathbf{y} = \mathbf{Z}\mathbf{x}. \tag{8}$$

Equation (8) can be solved by performing LU decomposition, after which the results of the LU-decomposed matrix $\mathbf{Z}$ can be used for solving the equation for an arbitrary propagation direction of the incident electromagnetic waves. This is useful for obtaining the optical parameters of randomly oriented particles.

Once $\mathbf{J}$ and $\mathbf{K}$ are obtained by solving Eq. (8) by using Eqs. (5) and (6), the vector scattering amplitude $\mathbf{F}$, the scattering cross section C_s, and the extinction cross section C_e are given by the optical theorem [20]:

$$\mathbf{F}(\mathbf{r}) = \frac{jk_0^2}{4\pi}\left[\mathbf{i}_r \times \xi\mathbf{i}_r \times \int_s \mathbf{J}\exp(jk_0\mathbf{r}' \cdot \mathbf{i}_r)\mathrm{d}s' + \mathbf{i}_r\right.$$

$$\left. \times \int_s \mathbf{K}\exp(jk_0\mathbf{r}' \cdot \mathbf{i}_r)\mathrm{d}s'\right], \tag{9}$$

$$C_s = \frac{1}{k_0^2A_0^2}\int|F|^2\mathrm{d}\Omega, \tag{10}$$

$$C_e = -\frac{4\pi}{k_0^2A_0^2}\mathrm{Im}\{\mathbf{A_0} \cdot \mathbf{F}(\mathbf{r_0})\}, \tag{11}$$

where $\mathbf{i}_r$ is a unit vector of the scattering direction $\mathbf{r}$ and A_0 is the polarized component of the incident electric field. Here, $\xi = \sqrt{\mu_0/\varepsilon_0}$, where $\mu_0 = 1.26 \times 10^{-6}$ [H/m] and $\varepsilon_0 = 8.85 \times 10^{-12}$ [F/m] are the permeability and the permittivity of vacuum, respectively.

C. Efficiency Factors and Size Parameters

The efficiency factors of extinction Q_{ext} and scattering Q_{sca} can be expressed in a simple manner as follows:

$$Q_{\mathrm{ext}} = C_e/(\pi r^2), \tag{12}$$

$$Q_{\mathrm{sca}} = C_s/(\pi r^2). \tag{13}$$

We defined r in Eqs. (12) and (13) as the radius of the sphere in the case of a spherical particle or that of an *equivalent-volume sphere* in the case of a nonspherical particle. The scattering properties are characterized by the ratio of the particle size and the wavelength λ of the electromagnetic wave. Thus, we defined the size parameter α as follows:

$$\alpha \equiv k_0 r = \frac{2\pi r}{\lambda}. \tag{14}$$

For example, $\alpha = 1$, 10, and 100 for a wavelength $\lambda \sim 3.7\,\mu m$ of shortwave infrared waves correspond to a particle radius of about 0.6, 6, and $60\,\mu m$, respectively. One of the shapes of particles targeted in this paper is that of a hexagonal column. The defined dimensions are illustrated in Fig. 2. In our definition, a hexagonal column is described by the lengths L and D, while the size parameters are defined as in Eq. (14).

In order to confirm validity of our SIEM/M algorithm we compared our result with the result appearing in Fig. 6(a) of Mano, under the same optical and particle conditions. Figure 3 shows the phase function of the hexagonal column obtained by the SIEM/M algorithm under the conditions of $\bar{m} = (1.3, -0.0)$, $L/D = 0.866$ (corresponding to $L/D = 1.0$ by the Mano definition), and $\pi L/\lambda = 3.4$. The result is quite similar to Mano, so that our calculation is consistent with that study.

3. Results

A. Accuracy with Respect to Q_{ext} versus NMNP

We assumed a wavelength of $3.7\,\mu m$ for the calculations since this wavelength is important for retrieving cloud particle size in the application of cloud remote sensing with visible-to-infrared imaging sensors. The extinction efficiency factor Q_{ext} of a homogeneous spherical particle was calculated with a
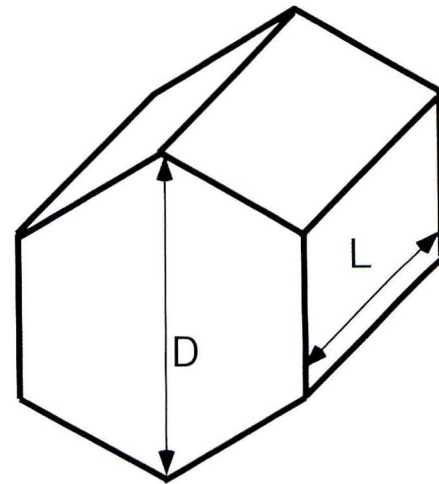

Fig. 2. Definition of the hexagonal column dimension. Aspect ratio is described by L/D.

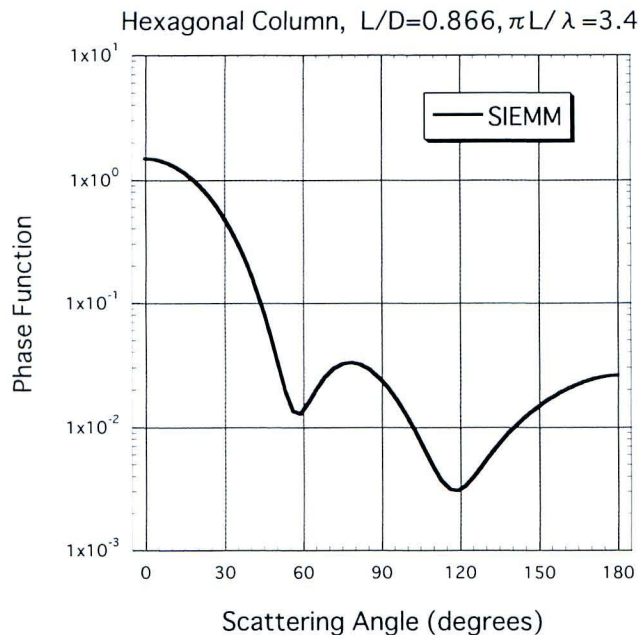## Hexagonal Column, L/D=0.866, $\pi L/\lambda$ =3.4

Fig. 3. Phase function of a hexagonal column obtained by SIEM/M. The obtained curve corresponds to that in Fig. 6(a) in Mano [16]. The conditions of the particle are $\tilde{m} = (1.3, -0.0)$, $L/D = 0.866$ (corresponding to $L/D = 1.0$ by the Mano definition), and $\pi L/\lambda = 3.4$.

complex index of refraction $\tilde{m} = (1.395, -6.99 \times 10^{-3})$ by assuming an ice-phase particle at a wavelength of 3.7 μm of the electromagnetic waves, for values of the parameter α in the range between 1 and 30. Figure 4 shows Q_{ext} as a function of the size parameter α [Figs. 4(a) and 4(b)], as well as the relative error of Q_{ext} as obtained with SIEM/M against the exact solution obtained from the Mie theory. The results are shown as a function of NMNP [Figs. 4(c) and 4(d)] for electromagnetic waves with polar incidence (PI) [Figs. 4(a) and 4(c)], and equator incidence (EI) [Figs. 4(b) and 4(d)]; Fig. 1 contains a definition of PI and EI. The relationships between the total NMNP and the number of nodes along the s and t curves are summarized in Table 1.

As shown in Fig. 4, Q_{ext} as obtained with SIEM/M is similar to an exact Q_{ext} when the size parameter is less than about 10, in the case of both PI and EI. The differences increase as the size parameter increases, and drastically decrease following the increase of NMNP. The errors decrease faster for PI than EI in most cases. Since these differences depend on the distribution of nodal points on the particle surface with respect to the direction of propagation of the incident light as well as total NMNP, the errors do not always linearly decrease with NMNP. However, the general trend is that Q_{ext} errors for PI appear to be smaller than those for EI. The oscillations of Q_{ext} along α are smoother for EI than for PI. This fact is due to the different distribution of nodal points with respect to the direction of propagation of the incident light. This feature is discussed in Subsection 3.B. by showing the electric currents $\mathbf{J}$ as obtained for the particle surface. Figures 4(c) and

4(d) show that the relative percent error of Q_{ext} decreases as NMNP increases. When NMNP = 3136 for PI and EI, the errors become 1% or less for values of size parameter α lower than about 20 and 17, respectively. On the basis of this evaluation, our SIEM/M is considered to be applicable for values of the size parameter lower than about 20, with an error of a few percent in the case of spherical particles. In this case, the node density was about four nodes per wavelength, as shown in Table 1. We also performed calculations without absorption $\tilde{m} = (1.395, -0.0)$ in order to estimate the convergence level of the calculations. The relative difference value of $|Q_{ext} - Q_{sca}|/Q_{ext}$ will be nearly zero if the calculation is precise. Here, the values were 6.7×10^{-4}, 2.3×10^{-3}, 6.6×10^{-3}, 1.0×10^{-2}, 2.0×10^{-2}, and 2.7×10^{-2} for values of the size parameter $\alpha = 1, 5, 9, 13, 17,$ and 21 when total NMNP = 2408, and were 4.9×10^{-4}, 2.1×10^{-3}, 6.3×10^{-3}, 9.5×10^{-3}, 1.4×10^{-2}, and 2.0×10^{-2} when total NMNP = 3136.

B. Electric Current on the Surface of a Particle and Scattering Phase Function

The electric and magnetic currents $\mathbf{J}$ and $\mathbf{K}$ are obtained by solving Eq. (8) with the aid of Eqs. (5) and (6). Figure 5 illustrates the real part of the obtained $\mathbf{J}$ on the surface of a spherical particle for (a) PI and (b) EI, with a complex index of refraction $\tilde{m} = (1.395, -6.99 \times 10^{-3})$. The color on the surface denotes the magnitude of $|\text{Re}(\mathbf{J})|$ normalized by its maximum value. The particle was rotated in such a way that the incident light illuminated the target from the front-right region of each viewgraph, as indicated with thick blue arrows in the figure. We can identify concentric ripples on the particle surface, which appeared when α was larger than 5, where the number of ripples increased as the size parameter α increased. The difference of the Q_{ext} accuracy between PI and EI as noted in Subsection 3.A. can be explained by considering the different distribution of nodal points with respect to the direction of propagation of the incident light. For PI, the density of nodes is higher at the "north pole," so that the incident light will be dealt with more efficiently. Moreover, the ripples were smoothly distributed on the surface of the particle since each wavefront and t curve shared the same central point. On the contrary, the distribution of nodes is coarse at the surface that faces the incident light, and the wavefronts have a rough structure for EI. Thus, the better accuracy of Q_{ext} for PI was obtained as a result of the density of nodes at the specific area and the smooth appearance of the electric and magnetic currents on the surface of the particle. Despite the better accuracy of Q_{ext} for PI as compared with that for EI, the oscillation phases of Q_{ext} as a function of α are smoother for EI than for PI, as seen in Fig. 4. This is due to the regular intervals between the nodal points along the s direction, which is in the direction of propagation in the PI case. As size parameter varies, this spacing is not able to adequately represent the propagating wave. It is
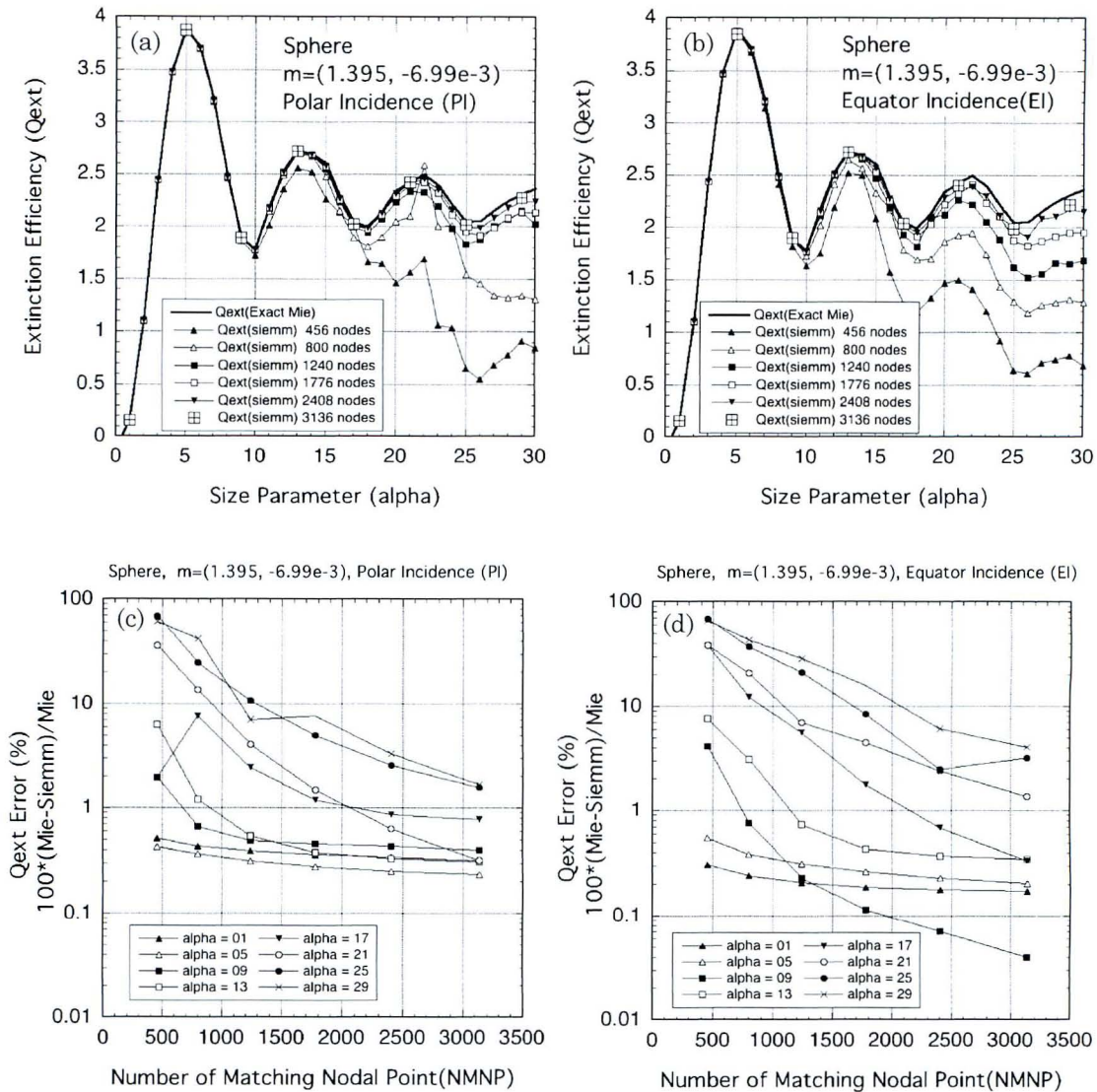
Fig. 4. (a), (b) Q_{ext} as a function of the size parameter α and (c), (d) relative error of Q_{ext} as obtained by SIEM/M against the exact solution obtained with the Mie theory as a function of the number of matching nodal point for electromagnetic waves with (a), (c) polar incidence and (b), (d) equator incidence.

remarkable that the EI case, for which the nodal points are more irregularly spaced in the direction of propagation, gives a smoother representation of the oscillation of Q_{ext} as a function of α. In general, however, the PI alignment is considered superior to the EI alignment for spherical particles. Our result indicates that the accuracy fluctuates in accordance
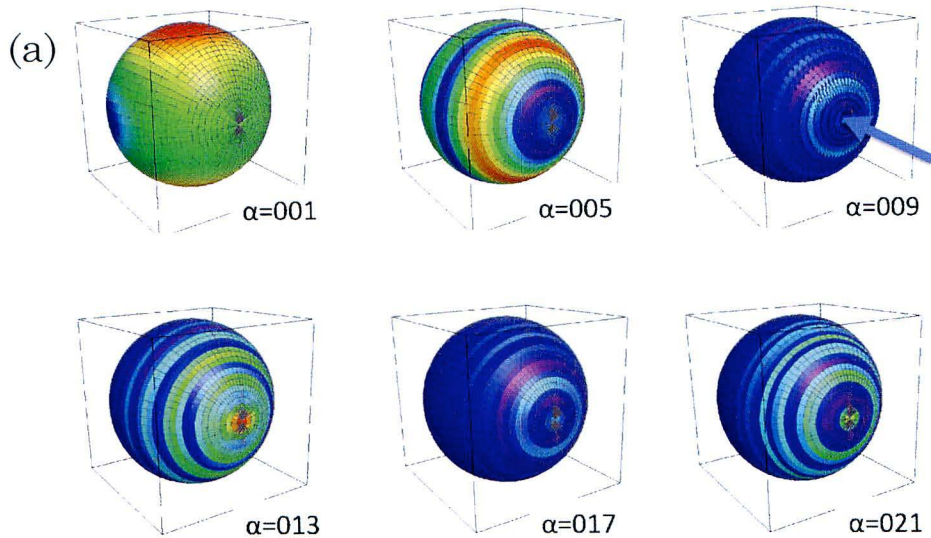
with the distribution of nodal points on the particle surface with respect to the direction of propagation of the incident light.

Figure 6 shows the phase functions for a sphere [Fig. 6(a)] and a hexagonal column with an aspect ratio L/D of 1.0 [Fig. 6(b)] for all scattering directions. The center and the circumference of each panel

Table 1. Average Number of Nodes per Wavelength Along s Parameter of the Spline Function at the Number of Matching Nodal Points

Total NMNP	NMNP along (s)	NMNP along (t)	Average Number of Nodes per Wavelength Along (s)							
			$\alpha = 1$	5	9	13	17	21	25	29
456	19	24	32.7	6.6	3.6	2.5	1.9	1.6	1.3	1.1
800	25	32	44.7	8.9	5.0	3.4	2.6	2.1	1.8	1.5
1240	31	40	56.7	11.3	6.3	4.4	3.3	2.6	2.3	2.0
1776	37	48	68.6	13.7	7.6	5.3	4.0	3.3	2.7	2.4
2408	43	56	80.6	16.1	9.0	6.2	4.7	3.8	3.2	2.8
3136	49	64	92.6	18.5	10.3	7.1	5.5	4.4	3.7	3.2

Re(J) on Sphere, m=(1.395,-6.99e-3), Polar Incidence (PI)

(a)

α=001   α=005   α=009

α=013   α=017   α=021

Re(J) on Sphere, m=(1.395,-6.99e-3), Equator Incidence (EI)
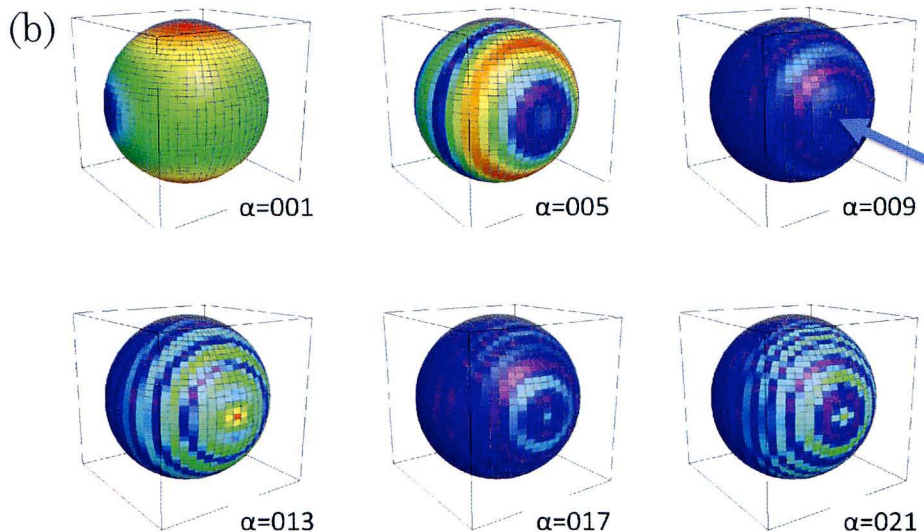

(b)

α=001   α=005   α=009

α=013   α=017   α=021

Fig. 5.   Real part of the obtained electric currents **J** for the spherical particle in the case of (a) polar incidence (PI) and (b) equator incidence (EI), with complex index of refraction $\bar{m} = (1.395, -6.99 \times 10^{-3})$. The particle was rotated in such a way that the incident light propagated toward the target particle from the front-right part in each viewgraph. The total number of matching nodal points is 3136.

denote forward and backward scattering, respectively. The values of the size parameter α are the same as those in Fig. 5. The total NMNP is 2408 ($=43 \times 56$) for the sphere and 2352 ($=49 \times 48$) for the hexagonal column, and the average number of nodes per wavelength along the s curve is 105.4, 21.1, 11.7, 8.1, 6.2, and 5.0 for values of size parameter $\alpha = 1, 5, 9, 13, 17,$ and 21 in the case of a hexagonal column. Since the number of nodes per wavelength is similar to that of a sphere with 2408 nodes, the calculation accuracy for a hexagonal column is considered to be similar to that for a sphere. In the case of a hexagonal column, the inci-

dent light propagates toward the particles along the z axis by adopting a fixed geometrical alignment (see Fig. 7). Rayleigh-like scattering (dipole scattering) occurs both in the case of a sphere and the case of a hexagonal column when the particle size is comparatively small (for example, when $\alpha = 1$). The phase function for the sphere becomes gradually isotropic as α increases, whereas the phase function for a hexagonal column for larger values of α has a more complex and distorted structure. The nonsphericity of the phase function appears around $\alpha \geq 3$ and gradually increases as α increases. The other difference between the characteristics of the phase function for

a sphere and a hexagonal column is the number and the locations of the "cold spots," where the phase function takes remarkably small values. When $\alpha = 17$, these spots appear at azimuth angles of $45°$, $135°$, $225°$, and $350°$ with elevation angles of $90°$ for a hexagonal column, and at $0°$, $90°$, $180°$, and $270°$ with elevation angles of $120°$ for a sphere.

4. Discussion of the Results for Randomly Oriented Particles

The scattering properties of a hexagonal column for different orientations of the particle with respect to the incident electromagnetic waves can be solved by controlling the terms $\mathbf{E}_{inc}$ and $\mathbf{H}_{inc}$ on the left side of Eqs. (1) and (2) since the particle orientation is

(a) Phase function for a Sphere, m=(1.395,-6.99e-3), Equator Inc. (EI)
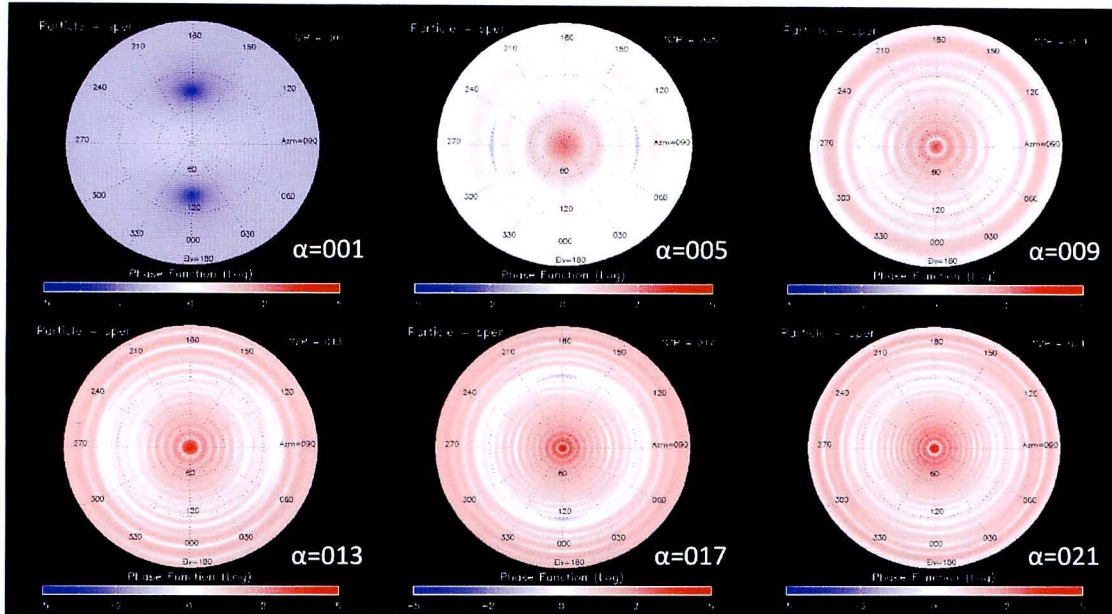
(b) Phase function for a Hexagonal Column, m=(1.395,-6.99e-3), Equator Inc. (EI)
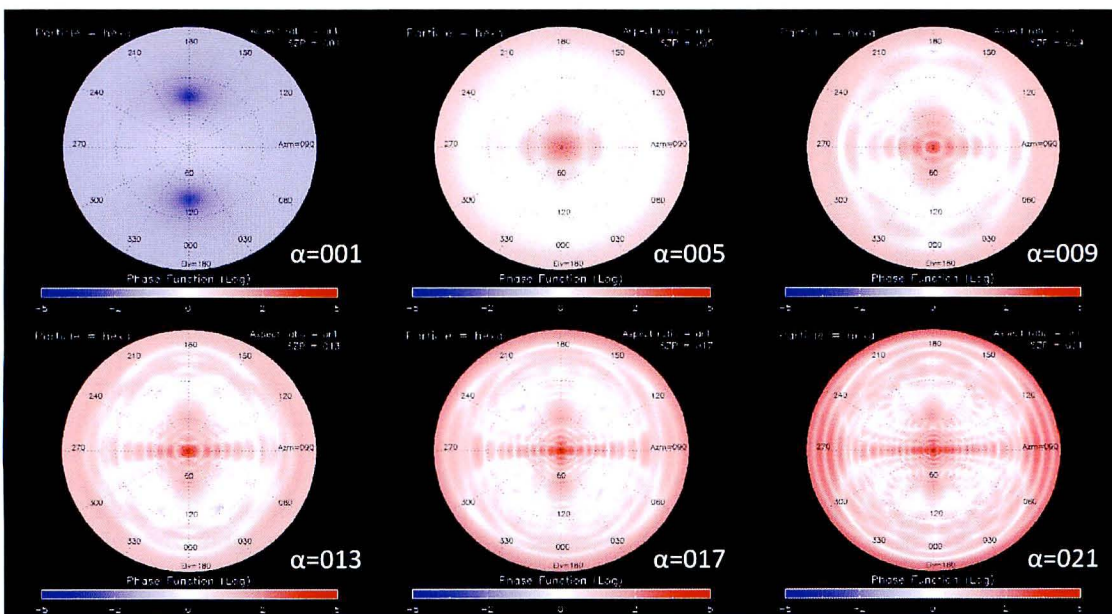

Fig. 6. Phase functions for (a) a sphere and (b) a hexagonal column with an aspect ratio of $L/D = 1.0$ for all scattering directions. The center and the circumference of each panel denote forward and backward scattering, respectively. The size parameters α are 1, 5, 9, 13, 17, and 21, with a refractive index $\bar{m} = (1.395, -6.99 \times 10^{-3})$. The total number of matching nodal points was 2408 ($=43 \times 56$) for the sphere and 2352 ($=49 \times 48$) for the hexagonal column.

equivalent to that of the incident electromagnetic waves. We specified the orientation of the particle with respect to the coordinate system by using two rotational angles. As a brief outline, a rotation around the z axis at an angle $\theta_z \in [0, 2\pi]$ and around the y axis at an angle $\theta_y \in [0, \pi]$ defines an arbitrary rotation of the target particle. In order to obtain the characteristic scattering features of a particle shaped as a hexagonal column, we obtained a solution with randomly oriented incident electromagnetic waves and averaged scattering properties. In order to estimate the degree of convergence, we defined a convergence parameter $\varepsilon \equiv |1 - \bar{Q}_{ext}(n+1)/\bar{Q}_{ext}(n)|$, where $\bar{Q}_{ext}(n)$ represents Q_{ext} averaged over the nth rotation. When $\varepsilon \leq 1.0 \times 10^{-4}$ consecutively five times, the calculation was terminated. A few hundred to thousand rotations were needed for $\alpha < 21$. Figure 8 illustrates the phase function P for values of the size parameter of (a) $\alpha = 1$, (b) 5, (c) 9, and (d) 21 of the sphere (Mie) and the hexagonal column (SIEM/M), where the complex index of refraction is $\tilde{m} = (1.313, -0.0)$, assuming an ice-phase particle and a wavelength of $0.5\,\mu m$ for the electromagnetic wave. For comparison of Mie and SIEM/M, the phase functions P were normalized by factor $c = 0.01$ and $c = 1.0$ for Mie and SIEM/M, respectively, using the formulation

$$P_{\text{normalized}} = c \times \frac{P}{\int P \sin\theta d\theta}, \qquad (15)$$

where θ is the scattering angle.

Fast oscillations in the phase function for each fixed orientation (see the results obtained by Mie) at relatively larger values of α weaken upon the averaging of the phase functions obtained in each randomly oriented in the case of a hexagonal column, with the exception of a noteworthy region around 20° for the scattering angle. The perturbations appearing in this angle interval are a well-known opti-
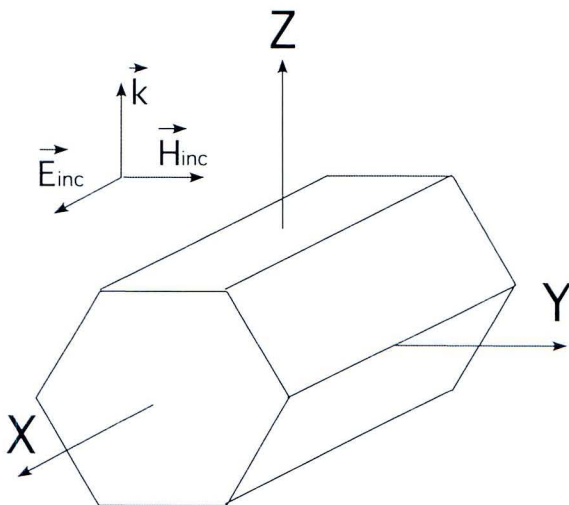
cal phenomenon referred to as "halo," which is a result of the hexagonal structure of the particle. Mishchenko et al. [21] investigated the phase function of circular cylinders by using T matrices and GOA and concluded that well-defined halo optical phenomena will appear when the value of the size parameter of a nonspherical particle is 100 and more. In this regard, a faint halo appeared slowly but steadily in the case of a hexagonal after a sufficiently high number of random reorientations. Similar results have been obtained with the FDTD method by Yang and Liou [13] for hexagonal columns with a size parameter of 10 and an aspect ratio of 2. The SIEM/M method also confirmed that a randomly oriented hexagonal particle generates a faint but noticeable signal for the halo phenomenon despite the relatively small particle size.

5. Summary and Concluding Remarks

A numerical calculation program based on a combined method involving SIEM/M was developed. In order to evaluate the accuracy of calculations with SIEM/M, we compared the scattering properties of spheres with respect to SIEM/M-derived and exact Mie solutions. The results showed that the accuracy depends on the NMNP and the error was lower than a few percent for NMNP of four or more per wavelength. It was shown that PI alignments yield more favorable solutions than EI alignments in most cases for spherical particles with the "latitude–longitude" type of node definition. This can be explained by the fact that the density of nodes is higher at the "north pole" so that the incident light will be dealt with more efficiently and the isotropic rippled structure of the electric and magnetic current on the surface of the particle was smooth in the case of PI and rough in the case of EI. It is shown that the calculation accuracy depends on the distribution of the nodal points on the surface with respect to the direction of propagation. Thus optimization of the node density with respect to the shape of the particle will be one of the tunable aspects in our algorithm.

A comparison of the respective phase functions for a sphere and a hexagonal column with a size parameter between 1 and 21 showed a Rayleigh-like scattering with comparatively small $\alpha \sim 1$ for both the sphere and the hexagonal column. Nonsphericity appeared in the phase function in the region of $\alpha \geq 3$ and gradually increased with the increase of α. Another difference in the characteristics of the phase function between a sphere and a hexagonal column was the number and the locations of "cold spots," at which the phase function takes remarkably small values.

An averaged phase function for a hexagonal column was obtained by solving SIEM/M. There appeared a remarkable optical phenomenon known as "halo" for scattering angles around 20° and relatively large values for the size parameter, such as 20. Our results suggested that the values of the size parameter at which halos appear are comparatively
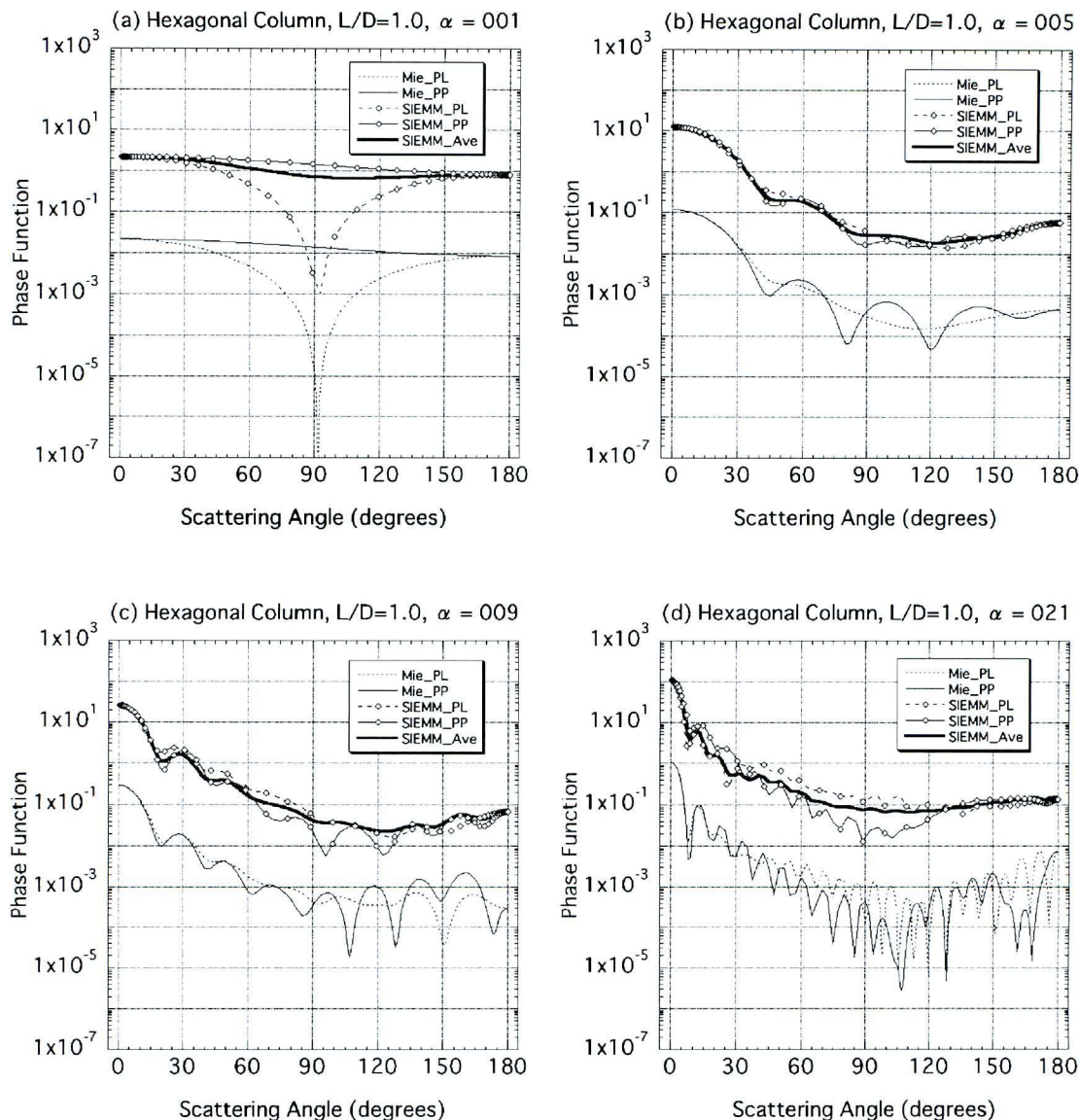

Fig. 7. Geometrical alignment of the incident electromagnetic waves and the hexagonal column used in Fig. 6.

Fig. 8. Phase function of Mie (lower curves) and hexagonal column particles with $L/D = 1.0$ (upper curves) with a size parameter (a) $\alpha = 1$, (b) 5, (c 9, and (d) 21. Phase functions were normalized by 0.01 (Mie) and 1.0 (SIEM/M). The complex index of refraction is $\tilde{m} = (1.313, -0.0)$. Phase functions parallel (thin dashed curves) and perpendicular (thin solid curves) to E_{inc} are shown. Azimuthally averaged results of the phase functions are also shown by thick solid curves.

smaller than previously considered. Until recently, the upper limit for the size parameter of SIEM/M was around 20 when using computers with ~8 gigabytes of memory, and this limit will increase following the increased availability of computer resources. Using the symmetric structure of the particles is expected to be an excellent way of increasing the size parameter. However, this study has been carried out from the perspective of applying this method to particles with arbitrary shape in the future with the aim that the computation holds for the full size of the scattering matrix [**Z** in Eq. (8)]. It is clear that this is a problem involving a trade-off between computer resources and degrees of asymmetry of the target particles. In part II of our paper, we will present some results of SIEM/M for particles with more complex shapes, with small to moderate size parameters.

Institute of Environmental Studies, Tsukuba, Japan (2006, 2007, 2008), and the Indian Space Research Organization (ISRO) Megha-Tropiques (MT) project.

References

1. K. N. Liou and Y. Takano, "Radiative transfer in cirrus clouds. Part III: Light scattering by irregular ice crystals," J. Atmos. Sci. **52**, 818–837 (1995).
2. A. Macke, "Scattering of light by polyhedral ice crystals," Appl. Opt. **32**, 2780–2788 (1993).
3. J. I. Peltoniemi, K. Lumme, K. Muinonen, and W. M. Irnine, "Scattering of light by stochastically rough particles," Appl. Opt. **28**, 4088–4095 (1989).
4. K. Muinonen, T. Nousiainen, P. Fast, K. Lumme, and J. I. Peltoniemi, "Light scattering by Gaussian random particles: ray optics approximation," J. Quant. Spectrosc. Radiat. Transfer **55**, 577–601 (1996).
5. A. Macke, M. I. Mishchenko, K. Muinonen, and B. E. Carlson, "Scattering of light by large nonspherical particles—approximation versus T-matrix method," Opt. Lett. **20**, 1934–1936 (1995).
6. P. Yang and K. N. Liou, "Light-scattering by hexagonal ice crystals—comparison of finite-difference time-domain and geometric optics models," J. Opt. Soc. Am. A **12**, 162–176 (1995).
7. P. Yang, H. L. Wei, H. L. Huang, B. A. Baum, Y. X. Hu, G. W. Kattawar, M. I. Mishchenko, and Q. Fu, "Scattering and absorption property database for nonspherical ice particles in the near- through far-infrared spectral region," Appl. Opt. **44**, 5512–5523 (2005).
8. G. Mie, "Beiträge zur Optik trüber Medien, speziell kolloidaler Metallösungen," Leipzig. Ann. Phys. **330**, 377–445 (1908).
9. J. R. Wait, "Scattering of a plane wave from a circular dielectric cylinder at oblique incidence," Can. J. Phys. **33**, 189–195 (1955).
10. S. Asano and G. Yamamoto, "Light scattering by a spheroidal particle," Appl. Opt. **14**, 29–49 (1975).
11. M. I. Mishchenko, L. D. Travis, and D. W. Mackowski, "T-matrix computations of light scattering by nonspherical particles: a review," J. Quant. Spectrosc. Radiat. Transfer **55**, 535–575 (1996).
12. M. I. Mishchenko, G. Videen, N. G. Khlebtsov, T. Wriedt, and N. T. Zakharova, "Comprehensive T-matrix reference database: a 2006–07 update," J. Quant. Spectrosc. Radiat. Transfer **109**, 1447–1460 (2008).
13. P. Yang and K. N. Liou, "Finite-difference time domain method for light scattering by small ice crystals in three-dimensional space," J. Opt. Soc. Am. A **13**, 2072–2085 (1996).
14. B. T. Draine and P. J. Flatau, "Discrete-dipole approximation for scattering calculations," J. Opt. Soc. Am. A **11**, 1491–1499 (1994).
15. B. T. Draine and P. J. Flatau, "Discrete-dipole approximation for periodic targets: theory and tests," J. Opt. Soc. Am. A **25**, 2693–2703 (2008).
16. Y. Mano, "Exact solution of electromagnetic scattering by a three-dimensional hexagonal ice column obtained with the boundary-element method," Appl. Opt. **39**, 5541–5546 (2000).
17. P. W. Zhai, C. H. Li, G. W. Kattawar, and P. Yang, "FDTD far-field scattering amplitudes: comparison of surface and volume integration methods," J. Quant. Spectrosc. Radiat. Transfer **106**, 590–594 (2007).
18. O. Dubovik, A. Sinyuk, T. Lapyonok, B. N. Holben, M. Mishchenko, P. Yang, T. F. Eck, H. Volten, O. Muñoz, B. Veihelmann, W. J. van der Zande, J.-F. Leon , M. Sorokin, and I. Slutsker, "Application of spheroid models to account for aerosol particle nonsphericity in remote sensing of desert dust," J. Geophys. Res. **111**, D11208 (2006).
19. C. Müller, *Foundations of the Mathematical Theory of Electromagnetic Waves* (Springer-Verlag, 1969).
20. J. D. Jackson, *Classical Electrodynamics* (Wiley, 1962)
21. M. I. Mishchenko and A. Macke, "How big should hexagonal ice crystals be to produce halos?," Appl. Opt. **38**, 1626–1629 (1999).